Photothermal Performance of 2D Material-Based Nanoparticles for Biomedical Applications

Amir Eghbali *, Nikolay V. Pak, Aleksey V. Arsenin, Valentyn Volkov, Andrey A. Vyshnevyy *

Posted Date: 13 May 2025

doi: 10.20944/preprints202505.0873.v1

Keywords: Photothermal therapy; light-to-heat conversion; optical absorption; plasmonic resonance

 doi:10.20944/preprints202505.0873.v1

Article

Photothermal Performance of 2D Material-Based Nanoparticles for Biomedical Applications

Amir Eghbali [1,*], Nikolay V. Pak [1,2], Aleksey V. Arsenin [2], Valentyn Volkov [2] and Andrey A. Vyshnevyy [1,2,*]

[1] Moscow Center for Advanced Studies, Kulakova str. 20, Moscow, 123592, Russia; amir.e.physics@gmail.com

[2] Emerging Technologies Research Center, XPANCEO, Internet City, Emmay Tower, Dubai, United Arab Emirates: pak.nv@xpanceo.com, arsenin@xpanceo.com, vsv@xpanceo.com

* Correspondence: amir.e.physics@gmail.com, vyshnevyy@xpanceo.com

Abstract: Photothermal therapy (PTT) is one of the rapidly developing methods for cancer treatment based on the strong light-to-heat conversion by nanoparticles. Over the past decade, the palette of photonic materials has expanded drastically, and nanoparticle fabrication techniques can now preserve the optical response of a bulk material in produced nanoparticles. This progress potentially holds opportunities for efficiency enhancement of PTT, not fully explored yet. Here we study the photothermal performance of spherical nanoparticles (SNs) composed of novel two-dimensional (2D) and conventional materials with existing or potential applications in photothermal therapy such as MoS_2, $PdSe_2$, Ti_3C_2, TaS_2 and TiN. Using the Mie theory, we theoretically analyze the optical response of SNs across various radii 5–100 nm in the near-infrared (NIR) region with a particular focus on the therapeutic NIR-II range (1000–1700 nm) and radii below 50 nm. Our calculations reveal distinct photothermal behaviors: large (radius > 50 nm) nanoparticles made of van der Waals semiconductors and $PdSe_2$ perform exceptionally well in the NIR-I range (750–950 nm) due to excitonic optical responses, while Ti_3C_2 nanoparticles achieve broad effectiveness across both NIR zones owing to its dual dielectric/plasmonic properties. Small TiN SNs excel in the NIR-I zone, owing to the plasmonic response of TiN at shorter wavelengths. Notably, a van der Waals metal TaS_2 emerges as the most promising photothermal transduction agent in the NIR-II region, particularly for smaller nanoparticles, due to its plasmonic resonance. Our insights lay a foundation for designing efficient photothermal transduction agents, with significant implications for cancer therapy and other biomedical applications.

Keywords: Photothermal therapy; light-to-heat conversion; optical absorption; plasmonic resonance

1. Introduction

Photothermal therapy (PTT) is an emerging and minimally invasive therapeutic technique that utilizes photothermal transduction agents (PTA) to convert light energy into heat for targeted tissue ablation [1,2]. This method has garnered significant interest for its potential applications in cancer treatment, where localized hyperthermia induced by PTAs can effectively destroy malignant cells while minimizing damage to surrounding healthy tissues [3]. The efficiency of PTT depends heavily on the properties of PTAs—such as their geometry, size, composition, and biocompatibility—as well as on the characteristics of the illuminating light, including its wavelength [4]. While noble metals are widely used in PTT, alternative plasmonic materials like transition metal nitrides (TMN), and van der Waals materials, such as transition metal dichalcogenides (TMDCs) and MXenes, whose atomic layers are weakly bound by van der Waals forces, offer several advantages, including lower toxicity [5], broad and tunable optical absorption [6], better photothermal stability [7] and cost-effectiveness [8].

 doi:10.20944/preprints202505.0873.v1

Among nanoparticle morphologies, spherical nanoparticles (SNs) are particularly favored due to their ease of synthesis, enhanced cellular uptake, and lower cytotoxicity [9–11]. Additionally, nanoparticle size plays a crucial role in determining both cellular uptake efficiency and clearance rate from the bloodstream. Studies indicate that SNs with a radius of 10–50 nm offer optimal cellular uptake and prolonged circulation, thereby maximizing therapeutic efficacy [12–14]. Moreover, SNs benefit from reduced aggregation. At the same time, the main disadvantage of uniform SNs is low tunability of optical response which depends only on a single size parameter. Novel materials may help to overcome this drawback by providing an additional degree of freedom.

The selection of the operating wavelength is crucial for optimizing PTT performance. The near-infrared (NIR) region is particularly advantageous due to its deep tissue penetration and reduced scattering [15]. Within this spectrum, two therapeutic windows are recognized, the first, NIR-I spans from 750 to 950 nm, while the second, NIR-II, lies slightly deeper into the near-infrared window from 1000–1700 nm [16]. NIR-II offers several benefits, including lower tissue absorption, reduced autofluorescence, and greater penetration depth [17,18]. These attributes make NIR-II an optimal spectral range for efficient photothermal heating, leading to improved therapeutic outcomes in biomedical applications. Over the last decade, considerable efforts have been spent to achieve stable production of highly crystalline SNs of van der Waals materials which preserve strong excitonic optical response of the initial crystal [19–22]. Hence, the material palette available for nanoparticle production has significantly expanded, complicating the choice of suitable material for PTT. Novel materials feature exotic optical properties, such as record-high refractive indices and strong optical absorption in the vicinity of excitonic resonances [23–25]. Their potential for theranostic applications is not yet fully understood.

Beyond PTT, enhancement of SNs optical absorption is desirable for diagnostics. In particular, the efficiency of photoacoustic imaging (PAI), a hybrid imaging modality that combines the high contrast of optical imaging with the deep tissue penetration of ultrasound [26,27], strongly depends on the absorption in the near-infrared (NIR) region.

In this work, we conduct a detailed theoretical investigation of spherical nanoparticles for photothermal therapy. We identify the most effective materials, including novel van der Waals materials, for specific nanoparticle sizes (radius ≤ 100 nm) and operating wavelengths within the near-infrared (NIR) range. Special attention is given to the NIR-II region and particle radii ≤ 50 nm to optimize safety and efficacy.

2. Methods

2.1. Model for Temperature Rise

At a steady state, where the temperature no longer changes with time in a solution containing SNs of radius R, the temperature increase (ΔT) due to nanoparticles is determined by the balance between energy absorption and heat dissipation in the surrounding medium. Mathematically, this relationship is given by:

$$\Delta T = \frac{Q_0 f_N V r}{NuAk}, \quad (1)$$

where $Q_0 = I_0\sigma_{abs}$ represents the energy absorbed by a single nanoparticle (Figure 1), where σ_{abs} is the absorption cross-section calculated using Mie theory [28] implemented in the self-written software. The incident radiation intensity I_0 is set to 3.2×10^5 W/m^2, and the nanoparticle concentration is given by $f_N = 4.24\times10^{14}(R_0/R)^3$ m^{-3} based on the conditions used by Rastinehad et al [29] for the tumor therapy. We choose the reference radius as $R_0 = 50$ nm. The solution's geometry is characterized by its volume (V), surface area (A), and characteristic length ($r = 1$ cm). The thermal conductivity of water is $k = 0.63$ W/(m·K), and the Nusselt number is approximated as $Nu \sim 5.3$.

2.2. Absorption Cross-Section of Small Spheres

When the nanoparticle radius R is much smaller than the wavelength of incident light ($\lambda/R \gg 1$), the electrodynamic effects of local-field enhancement become independent of the particle size. In this regime, retardation effects leading to radiative plasmon damping are negligible, and absorption

 doi:10.20944/preprints202505.0873.v1

is dominated by dipole interactions. The absorption cross-section can thus be expressed analytically using static dipole polarizability of a dielectric sphere, given by [30,31]:

$$\alpha = 3\varepsilon_0 V_0 \frac{\varepsilon - \varepsilon_h}{\varepsilon + 2\varepsilon_h}. \quad (2)$$

Here, V_0 is the volume of the particle, and ε represents the complex dielectric function of the particle material, while ε_h is the dielectric constant of the host medium. The absorption cross-section follows as:

$$\sigma_{\text{abs}} = \frac{\frac{1}{2}\text{Re}(-i\omega\alpha \mathbf{E}_0 \cdot \mathbf{E}^*)}{\frac{1}{2}\text{Re}(E_0 H_0^*)} = V_0 \frac{2\pi \text{Im}(\varepsilon)}{\lambda} \frac{9\varepsilon_h^{3/2}}{(\text{Re}(\varepsilon) + 2\varepsilon_h)^2 + \text{Im}(\varepsilon)^2}, \quad (3)$$

where $\mathbf{E}_0$, $\mathbf{H}_0$ and $\mathbf{E}$ are complex amplitudes of electric and magnetic fields of the incident wave and the electric field inside the nanoparticle, respectively. Equation (3) indicates that the absorption cross section is directly proportional to the volume of the particle, and it is related to the electrical conductivity σ of the particle material:

$$\sigma = \varepsilon_0 \frac{2\pi c}{\lambda} \text{Im}(\varepsilon), \quad (4)$$

and field enhancement:

$$\frac{|E|^2}{|E_0|^2} = \left|1 - \frac{\alpha}{3\varepsilon_0 V_0}\right|^2 = \frac{9\varepsilon_h^2}{[\text{Re}(\varepsilon) + 2\varepsilon_h]^2 + \text{Im}(\varepsilon)^2}. \quad (5)$$

Rearranging Equation (3) yields a more geometric-friendly form:

$$[\text{Re}(\varepsilon)]^2 + [\text{Im}(\varepsilon) - b/\sigma_{\text{abs}}]^2 = (b/\sigma_{\text{abs}})^2, \quad (6)$$

where b is

$$b = 9V_0 \pi \varepsilon_h^{3/2}/\lambda. \quad (7)$$

Equation (6) reveals that, in the (Re(ε), Im(ε))-plane, the geometric locus of a constant absorption cross-section (σ_{abs}) is a circle with a radius of b/σ_{abs}, and a center at ($-2\varepsilon_h$, b/σ_{abs}). This geometric representation provides a powerful tool for visualizing absorption behavior, aiding in the identification of optimal material properties and wavelengths for small sizes. Note that even for small nanospheres, Equation (3) has limited applicability close to the plasmonic resonance $\varepsilon = -2\varepsilon_h$, where it formally yields an infinite absorption cross-section. In our work, Im(ε) is much larger than $(2\pi R/\lambda)^3$, so Equation (3) is accurate.

3. Results and Discussion

We evaluate the photothermal response of spherical nanoparticles in water [32] (Figure 1) using five different nanoparticle materials—TaS_2 [25], MoS_2 [24], $PdSe_2$ [33], Ti_3C_2 [34], TiN [35]—selected for their distinct optical properties, making them promising for photothermal therapy.

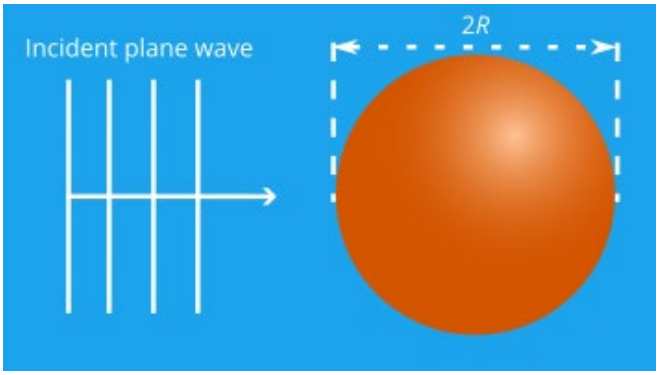

Figure 1. A plane wave incident upon a spherical nanoparticle of radius R embedded in a transparent medium.

 doi:10.20944/preprints202505.0873.v1

3.1. Optical Heating Patterns

To put the performance of different materials into the same perspective, we calculated the temperature rise of nanoparticles having the same wavelength-to-radius ratios λ/R as a function of complex refractive index $\varepsilon = \mathrm{Re}(\varepsilon) + i\mathrm{Im}(\varepsilon)$. For details on the calculations see Methods. The calculation results, presented in Figure 2, reveal the formation of hot zones related to resonant heating, a phenomenon where an incident wave efficiently couples to a nanoparticle eigenmode. This coupling leads to the enhanced local electric field, hence an increased optical absorption. Note that when the $\mathrm{Im}(\varepsilon)$ is smaller, the field enhancement is stronger due to the higher Q-factor of the corresponding resonance, however too small $\mathrm{Im}(\varepsilon)$ will diminish optical absorption. Therefore, the maximum optical absorption is achieved at an optimal value of $\mathrm{Im}(\varepsilon)$ at which radiative losses and absorption losses become equal [36].

Within our study range of particle radii from 5 to 100 nm and operating wavelengths from 650 to 1500 nm, ratio $\lambda/R = 9$ and 100 correspond to large and small nanoparticles, respectively. Also, we added $\lambda/R = 16$ as a transitional case between these two extremes.

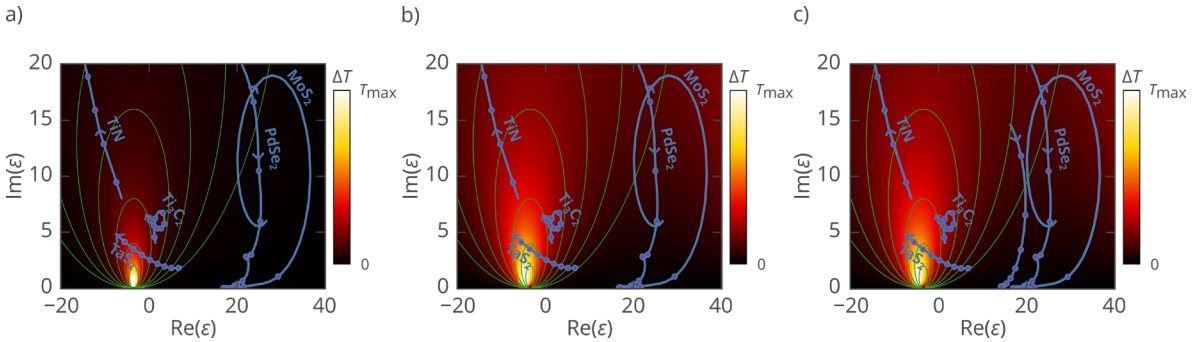

Figure 2. Calculated heating maps for spherical nanoparticles in water (refractive index: 1.327 [32]) with fixed wavelength(λ) to radius(R) ratios for different real and imaginary parts of permittivity: (**a**) $\lambda/R = 100$, (**b**) $\lambda/R = 16$ and (**c**) $\lambda/R = 9$. Directed blue lines depict dispersion $\varepsilon(\lambda)$ of different materials. Arrow directions correspond to the increase in wavelength from 650 nm to 1500 nm. Consecutive dots are 100 nm of wavelength apart. Thin green lines are lines of equal absorption within the static approximation plotted according to Equation (6).

For $\lambda/R = 100$ (Figure 2a), a single electric dipole resonance with $\mathrm{Re}(\varepsilon) \approx -3.5$ is observed which represents a localized surface plasmon resonance. The absorption pattern for this ratio aligns well with the predictions of Equation (3).

For $\lambda/R = 16$ (Figure 2b), the same resonance is observed but shows slightly weaker agreement with Equation (3) due to the increased influence of radiative losses which are not accounted for by the static approximation. Additionally, a trace of the magnetic dipole (MD) resonance is evident near the boundary of the simulation domain.

For $\lambda/R = 9$ (Figure 2c), the larger size of the structure relative to the wavelength leads to the occurrence of multiple resonances. When a material's excitonic resonance in dielectric function is close to the Mie resonance hotspot it results in Mie-resonance-enhanced optical absorption. At $\mathrm{Re}(\varepsilon) \approx -3.5$, both electric dipole (ED) and electric quadrupole (EQ) plasmonic resonances are observed. MD resonance appears at $\mathrm{Re}(\varepsilon) \approx 20$, and at $\mathrm{Re}(\varepsilon) \approx 40$, both ED and magnetic quadrupole (MQ) resonances are present. The optimal $\mathrm{Im}(\varepsilon)$ values for dipole mode resonances are higher than those of $\lambda/R = 16$ and 100, due to increased radiative losses associated with larger relative sizes.

To get a general sense of how various 2D materials perform across different sizes and wavelengths, we analyze the electric permittivity curves of the materials in Figure 2. Performance of small nanoparticles (Figure 2a) is dictated by how far the material properties are from the plasmonic resonance. In this regard, MoS_2 and $PdSe_2$ nanoparticles demonstrate low optical absorption. In contrast, the dispersion lines of TaS_2 (at $\lambda \approx 1300$ nm), Ti_3C_2 (at $\lambda \approx 700$, 1500 nm), and TiN (at $\lambda \approx 650$ nm) pass close to the resonance, resulting in strong absorption.

As follows from Figure 2c, large nanoparticles are capable of Mie-resonance enhanced optical absorption. In particular, MoS_2 nanoparticles support MD resonance ($\mathrm{Re}(\varepsilon) \approx 20$), followed by ED resonance ($\mathrm{Re}(\varepsilon) \approx 40$) at $\lambda \lesssim 700$ nm. $PdSe_2$ nanoparticle heating is due to the MD resonance, which

 doi:10.20944/preprints202505.0873.v1

is particularly pronounced in the 800–1000 nm range. Meanwhile, the optical absorption of TaS_2 ($\lambda \approx$ 1300 nm), Ti_3C_2 ($\lambda \approx$ 700, 1500 nm), and TiN ($\lambda \approx$ 650 nm) nanoparticles is again due to plasmonic resonances (Re(ε) ≈ −3.5).

3.2. Performance of 2D Materials for Photothermal Therapy and Imaging

To facilitate a systematic analysis and comparison of the 2D materials mentioned before—TaS_2, MoS_2, $PdSe_2$, Ti_3C_2, and TiN—we divide the wavelength range into NIR-I and NIR-II regions, while particle sizes are grouped as large ("L": $R > 50$ nm) or small ("S": $R \leq 50$ nm). This classification creates four distinct zones on the radius-wavelength space: L-NIR-I, S-NIR-I, L-NIR-II, and S-NIR-II. In Figure 3 we plot the top-performing 2D materials and their temperature increase (ΔT) across these zones (σ_{abs}/V_0 as a function of R and λ are included in Supplementary Table S1). For effective PTT, it is required that the tissue temperature reaches about 50 °C, which translates to a temperature rise ΔT of less than 20 °C [37]. As can be seen from Figure 3, studied materials easily surpass this threshold. Meanwhile, Figure 4 demonstrates the heating performance of different materials for large (R = 100 nm) and small (R = 35 nm) nanoparticles within both NIR-I & NIR-II regions. Below, we assess the performance of each 2D material, based on the data presented in Figures 2, 3, and 4.

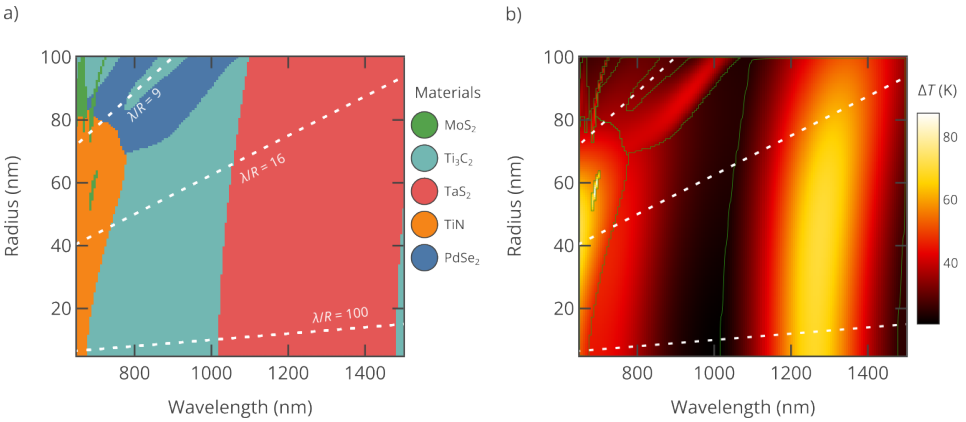

Figure 3. (**a**) Color map of the best-performing materials across radii ranging from 5 nm to 100 nm and wavelengths spanning 650 nm to 1500 nm. (**b**) Heating map for the selected materials. The green lines in panel (b) separate the areas of different materials. Dashed lines in panels (a) and (b) correspond to constant λ/R ratios in Figure 2.

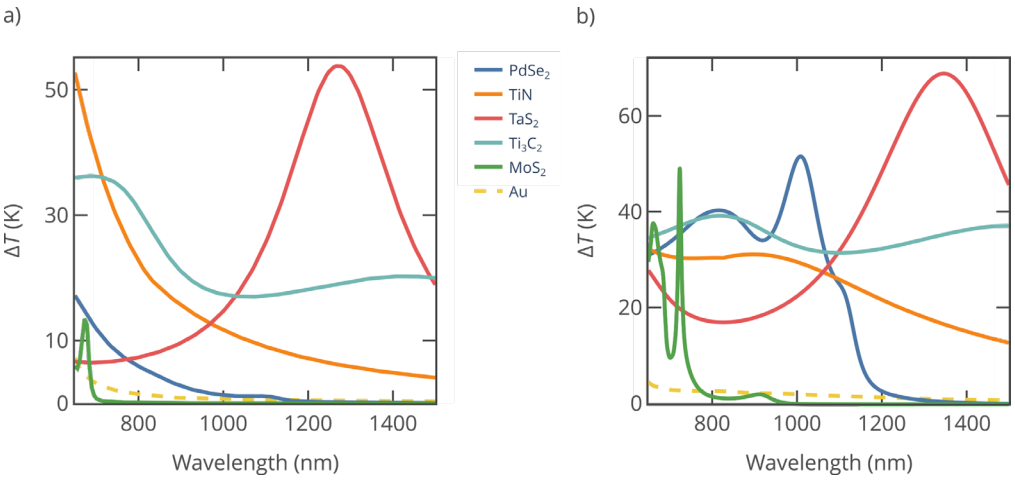

Figure 4. Heating as a function of wavelength for nanoparticles with radii of (**a**) R = 35 nm and (**b**) R = 100 nm, composed of various materials. For comparison we added gold nanospheres of the same radii. The host medium is water.

MoS_2 and other semiconducting TMDCs. MoS_2, a two-dimensional TMDC, exhibits pronounced excitonic effects due to its reduced dimensionality and strong Coulomb interactions

 doi:10.20944/preprints202505.0873.v1

[24,25]. Strong excitonic resonance manifests as the large loop in Re(ε)-Im(ε) plane showing the strong absorption and high dielectric constant. As a result, with this material it is possible to achieve Mie-resonance assisted optical absorption which requires the nanoparticle radius to be larger than 50 nm (Figure 3a). In this case, nanoparticles efficiently support ED, MD, and QD resonances. Other semiconducting TMDC, e.g., WS_2, WSe_2, $MoSe_2$, $MoTe_2$ show similar behavior [23,25], with excitonic resonances in NIR-I and no noticeable absorption in NIR-II which is below their bandgap. Consequently, MoS_2 and other TMDCs are best in narrow wavelength regions in the L-NIR-I zone. At the same time, they should be used with caution. Sharp Mie resonances of MoS_2, shown in Figure 4, are vulnerable to inherent polydispersion of SNs. In PTT applications MoS_2 nanoparticles may benefit from remarkable photothermal stability [19].

$PdSe_2$. Similarly to semiconducting TMDCs, $PdSe_2$ exhibits pronounced excitonic peaks, as reported in previous studies [25], with excitonic transitions forming a distinct arch in its dielectric function line in Figure 2. In the NIR-I window and the early NIR-II, larger $PdSe_2$ nanoparticles effectively sustain both MD and ED resonances. Although recent analysis of $PdSe_2$ optical and electronic properties established that it is a semimetal [38], due to the momentum mismatch between semimetallic bands, its optical behavior in the near-infrared spectral range is closer to TMDC semiconductors rather than other van der Waals semimetals such as graphene. As a result, like other TMDC semiconductors, $PdSe_2$ demonstrates strong performance in the L-NIR-I zone.

TiN. TiN is not a van der Waals material but has attracted great interest for decades owing to its high melting point, chemical durability and good conductivity which makes it an "alternative plasmonic material" [39]. The TiN dielectric function crosses zero in the visible range, making it plasmonic in the NIR spectra region, hence attractive for PTT [40]. TiN SNs also show low cytotoxicity and high photothermal stability [40]. Furthermore, the dielectric function shifts away from the heating hotspots in Figure 2 as the wavelength increases. These characteristics explain why TiN exhibits its superior performance primarily in the S-NIR-I zone.

On the side note, many traditional plasmonic materials, such as noble metals and aluminum undergo plasmonic transition deep in the visible range or even UV, so their uniform spherical nanoparticles perform quite badly as PTT agents. As seen from Figure 4, uniform gold nanoparticles yield temperature rise of less than 10 K throughout the whole NIR spectral region. To improve the performance, core-shell nanoparticles [29] or hollow gold shells [41] should be employed which require more sophisticated fabrication protocols [42]. The improvement in the optical absorption comes at a price of increased size—specially designed gold nanoshell particles (Auroshell) for PTT therapy have a diameter of about 150 nm [29].

Ti_3C_2. Ti_3C_2 belongs to MXenes, layered materials obtained by etching of MAX-phases [43] where M denotes metal, A is an A-group atom, X is carbon or nitrogen. As shown in Figure 2, the Ti_3C_2 dielectric function line features a loop associated with interband transitions [34], followed by Re(ε) zero crossing near 1400 nm signifying its metallic nature. As a result, optical absorption of Ti_3C_2 nanoparticles in the near-infrared (NIR) region is due to proximity to localized plasmonic resonance. In the L-NIR-I area, they also benefit from magnetic dipole (MD) response. The dual dielectric/plasmonic response makes Ti_3C_2 effective across all four zones: L-NIR-I, L-NIR-II, S-NIR-I and S-NIR-II. Cytotoxicity studies of Ti_3C_2 MXene sheets shows that they are more harmful to cancer cells than to normal ones [44]. Overall, the biocompatibility of Ti_3C_2 nanoparticles requires additional studies since the chemical activity and surface groups may change during nanoparticle synthesis.

TaS_2. Unlike transition metal dichalcogenides composed of group IVB and VIB transition metal atoms, TaS_2 exhibits metallic behavior [45,46]. Tantalum is a biocompatible material; tantalum compounds are in medical use for more than 50 years [47]. Recent studies of PEG-TaS_2 nanosheets demonstrated no significant cytotoxicity after 24–48 h incubation [48]. As illustrated in Figure 2, Re(ε) for TaS_2 transitions from positive to negative near 1100 nm, indicating a free-electron response [25]. Unlike Ti_3C_2, interband transitions in TaS_2 peak in ultraviolet range and do not influence photoresponse in NIR. Furthermore, among the materials with Re(ε) < 0 whose dispersion curves were plotted in Figure 2, TaS_2 demonstrates the lowest Im(ε), attributed to its uniquely low density of scattering states in the NIR, a result of its distinctive electronic band structure [45]. The combination of low Im(ε) and the dielectric function curve passing through Re(ε) = $-2\varepsilon_h$ gives rise to an

 doi:10.20944/preprints202505.0873.v1

unparalleled plasmonic absorption peak in the NIR-II region, which is responsible for the remarkable performance of TaS_2 nanoparticles in the L-NIR-II and S-NIR-II zones. Broadband optical absorption of TiN, Ti_3C_2 and TaS_2 ensures their stable performance even if SNs have wide dispersion of sizes.

SNs that strongly absorb light can have other applications beyond PTT. The same optical properties that make nanoparticles effective for PTT—such as their strong absorption in the NIR region—also make them well-suited for PAI, enabling simultaneous therapeutic and diagnostic applications.

3.3. In-Depth Study of S-NIR-II Zone

To deepen our understanding of the physics underlying the S-NIR-II zone, we conduct a detailed investigation of TaS_2—the most promising material among the examined 2D candidates. Our analysis unfolds in three stages. First, we compare the heating spectra obtained from both Equation (3) and Mie theory. Finally, we introduce a phenomenological model, drawing inspiration from Equations (3-6) and the underlying physics, to describe and explain the general behavior of the TaS_2 nanoparticle in S-NIR-II.

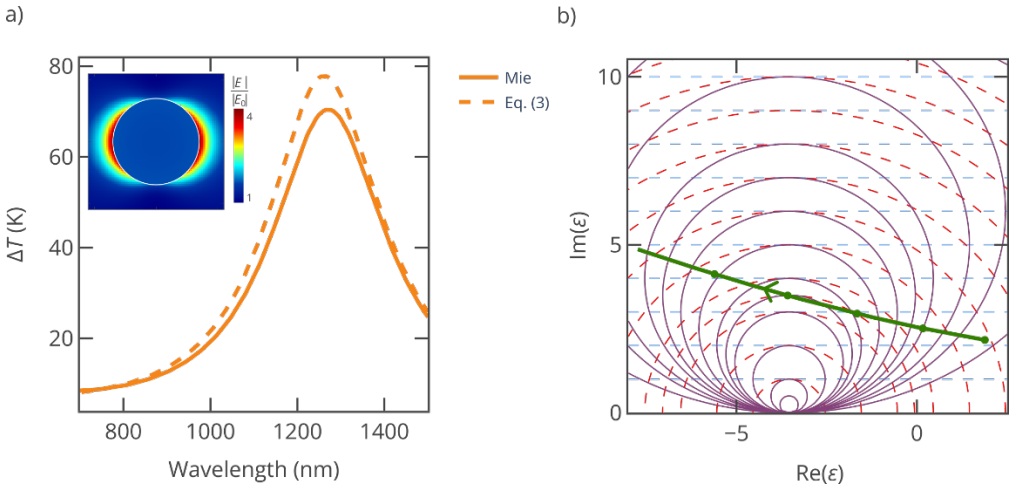

Figure 5. (**a**) Heating calculated using Mie theory for a nanoparticle with R = 35 nm (solid line) and Equation (3) (dashed line). The inset shows the electric field enhancement at λ = 1272 nm. (**b**) Directed blue green line depicts dispersion $\varepsilon(\lambda)$ of TaS_2 in Re(ε)-Im(ε) plane. The arrow direction corresponds to the increase in λ from 1000 nm to 1500 nm. The solid purple lines are lines of equal absorption within the static approximation plotted according to Equation (6). The dashed blue lines are the lines of constant electrical conductivity (Equation (4)). The dashed red lines are the lines of constant electric field enhancement (Equation (5)).

The heating curve obtained from Equation (3) exhibits a peak temperature rise of ΔT = 78 K at a wavelength of λ = 1261 nm, while the exact curve calculated from the Mie theory shows a peak of ΔT = 70 K at λ = 1272 nm (Figure 5a). In the inset, we have the electric field enhancement at λ = 1272 nm. Given the small nanoparticle radius (R = 35 nm), the result from Equation (3) closely aligns with that of Mie theory. The observed blue shift in the peak position of Equation (3) relative to Mie theory, along with its higher temperature rise, can be attributed to the quasistatic approximation used in Equation (3), which neglects radiation losses and dynamic depolarization [49]. Indeed, according to the long-wavelength approximation [50] the plasmonic resonance occurs at $\varepsilon/\varepsilon_h = -2 - 2.4\varepsilon_h(2\pi R/\lambda)^2$ which has a lower real part of dielectric permittivity hence is attained at a slightly higher wavelength.

As the wavelength increases, the TaS_2 dispersion curve crosses purple circles in Figure 5b with progressively smaller radii which means higher absorption cross section. However, between 1200 nm and 1300 nm, this trend reverses, indicating that the absorption peak wavelength lies within this interval. A similar pattern emerges with the dashed red circles in Figure 5b which indicate the field enhancement: as the wavelength increases, the TaS_2 dispersion curve moves toward smaller radii but again reverses between 1200 nm and 1300 nm, locating the highest field enhancement resonance in this same wavelength range. An increase in Im(ε), represented by the dashed blue lines in Figure 5b,

 doi:10.20944/preprints202505.0873.v1

intensifies ohmic losses within the nanoparticle, reducing the internal-to-incident electric field ratio. As illustrated in the inset of Figure 5a, while significant field enhancement of $|E|/|E_0| = 4$ occurs around the nanoparticle surface at $\lambda = 1272$ nm, the internal field enhancement remains weak with $|E|/|E_0| = 1.6$.

It should be noted that Figure 5b should not be used for exact determination of the absorption peak, e.g., by finding the purple circle tangent to the dispersion line. According to Equations (6,7) the absorption associated with the circle is wavelength-dependent so a larger circle can correspond to higher absorption if the wavelength is sufficiently smaller, thus the exact maximum is slightly blue-shifted from the tangent point. Nonetheless, it is useful for illustration of the underlying physical mechanisms driving the optical absorption in small nanoparticles.

The performance of small nanospheres is eventually determined by how small $\mathrm{Im}[\varepsilon(\omega)]$ is when $\mathrm{Re}[\varepsilon(\omega)] = -2\varepsilon_h$. It is instructive to roughly estimate the lower limit on $\mathrm{Im}(\varepsilon)$. In the visible and near-infrared range, negative permittivity is achieved thanks to free electron gas in metallic materials [51]. Dispersion law of these materials is usually described by $\varepsilon(\omega) = \varepsilon_b(\omega) - \omega_p^2/(\omega^2 + i\Gamma\omega)$, where $\varepsilon_b(\omega)$ is the contribution of bound electrons, and the second term is free carrier response, with ω_p and Γ being the plasma frequency and scattering rate. The plasmonic resonance is determined by the condition $-2\varepsilon_h = \mathrm{Re}(\varepsilon_b) - \omega\omega_p^2/(\omega^3 + \Gamma^2\omega)$. At the same time, $\mathrm{Im}(\varepsilon) = \mathrm{Im}(\varepsilon_b) + \Gamma\omega_p^2/(\omega^3 + \Gamma^2\omega)$, from which we immediately get $\mathrm{Im}(\varepsilon) = \mathrm{Im}(\varepsilon_b) + [2\varepsilon_h + Re(\varepsilon_b)]\Gamma/\omega$. From this equation, it is easy to see conditions which must be met to achieve minimal $\mathrm{Im}(\varepsilon)$. First, no interband transition channels should be present to ensure $\mathrm{Im}(\varepsilon_b) = 0$. Second, Γ should be as small as possible. This value is determined by electron-phonon interaction and electron-electron scattering, and, although they depend on details of electron-phonon and electron-electron coupling and electronic density of states, a good estimate is $\Gamma = 8\times10^{13}$ s^{-1}, which corresponds to the best performing gold films [52]. Finally, one must achieve minimal $\mathrm{Re}(\varepsilon_b)$, ideally, close to 1. The main difficulty is that the influence of optical transitions at characteristic frequency ω_{tr} on $\mathrm{Re}(\varepsilon)$, according to the Kramers–Kronig relations [53], decays as $1/(\omega_{tr}-\omega)$, and may result in high $\mathrm{Re}(\varepsilon_b)$ even far from the interband absorption edge. A prominent illustration of this principle is MoS_2 which has $\varepsilon \approx 17$ in the near-infrared range. Assuming minimal possible $\mathrm{Re}(\varepsilon_b) = 1$ and $\mathrm{Im}(\varepsilon_b) = 0$, we get $\mathrm{Im}(\varepsilon) > 0.25$ at a wavelength of 1300 nm corresponding to the center of the NIR-II band. This value is an order of magnitude below that for TaS_2 which gives a modest hope that even better materials for theranostic applications can be found in the future.

4. Conclusions

This study presents a comprehensive theoretical analysis of the photothermal response of spherical nanoparticles (SNs) composed of promising materials—TaS_2, MoS_2, $PdSe_2$, Ti_3C_2, and TiN—across various sizes and near-infrared (NIR) wavelengths. These materials represent the families of TMDC semiconductors, MXenes, alternative plasmonic materials and two-dimensional metals and semimetals. Our findings reveal distinct photothermal performance across different materials and spectral zones: MoS_2 (and other TMDC semiconductors) excel in the L-NIR-I zone due to its exciton-driven effects, enabling strong magnetic dipole (MD), electric dipole (ED), and quadrupole (QD) resonances. $PdSe_2$ also performs well in the L-NIR-I zone, driven by pronounced excitonic peaks and a metallic Drude response that enhances MD and ED resonances. TaS_2 emerges as the top performer in the NIR-II region, particularly for smaller nanoparticles, owing to its unique plasmonic absorption properties and minimal radiative losses. Ti_3C_2 demonstrates versatility across all spectral zones, supported by its dual dielectric/plasmonic response and interband transitions, while TiN shows superior performance in the S-NIR-I zone due to its plasmonic response at shorter wavelengths.
Among these materials, a van der Waals metal TaS_2 stands out as the most promising candidate for photothermal therapy (PTT), achieving optimal photothermal heating efficiency in the NIR-II region. The theoretical framework developed in this study provides critical insights into the design of efficient photothermal transduction agents, underscoring the importance of material selection, nanoparticle size, and wavelength optimization. These findings advance the potential of PTT, particularly in cancer treatment, by enabling localized hyperthermia that selectively targets malignant cells while sparing healthy tissues. This research can be further developed in the direction

 doi:10.20944/preprints202505.0873.v1

of TaS_2 and Ti_3C_2 nanoparticles fabrication and testing their photothermal conversion, cytotoxicity and biocompatibility, followed by in vivo PTT study. Also, we predict the possibility of other materials which can outperform TaS_2. This work paves the way for the development of next-generation photothermal transduction agents with enhanced therapeutic efficacy.

Supplementary Materials: The following supporting information can be downloaded at: https://www.mdpi.com/article/doi/s1, Table S1: σ_{abs}/V_0 spectra (m^{-1}) for different materials;

Author Contributions: Conceptualization, A.A.V, A.V.A; methodology, A.A.V., V.V.; software, A.E, A.A.V.; investigation, A.E., N.V.P.; writing—original draft preparation, A.E.; writing—review and editing, N.V.P., A.A.V; supervision, A.V.A., V.V., A.A.V.; funding acquisition, A.A.V. All authors have read and agreed to the published version of the manuscript.

Data Availability Statement: The original contributions presented in the study are included in the article; further inquiries can be directed to the corresponding authors.

Conflicts of Interest: The authors declare no conflicts of interest. The funders had no role in the design of the study; in the collection, analyses, or interpretation of data; in the writing of the manuscript; or in the decision to publish the results.

Funding: A.E.: N.V.P. and A.E. acknowledge support by the Russian Science Foundation grant 22-79-10312.

References

1. Sharma, S.; Batra, S.; Chauhan, M.K.; Kumar, V. Photothermal Therapy for Cancer Treatment. In *Biological and Medical Physics, Biomedical Engineering*; Biological and Medical Physics, Biomedical Engineering; Springer Nature Singapore: Singapore, 2023; pp. 755–780 ISBN 9789811997853.
2. Hong, F.; Geng, X.; Min, G.; Sun, X.; Zhang, B.; Yao, Y.; Li, R.; Wang, J.; Zhao, H.; Guo, P.; et al. Deep NIR-II Optical Imaging Combined with Minimally Invasive Interventional Photothermal Therapy for Orthotopic Bladder Cancer. Chem. Eng. J. **2022**, 449, 137846.
3. Xie, X.; Gao, W.; Hao, J.; Wu, J.; Cai, X.; Zheng, Y. Self-Synergistic Effect of Prussian Blue Nanoparticles for Cancer Therapy: Driving Photothermal Therapy and Reducing Hyperthermia-Induced Side Effects. *J. Nanobiotechnology* **2021**, *19*, 126.
4. Jaque, D.; Martínez Maestro, L.; del Rosal, B.; Haro-Gonzalez, P.; Benayas, A.; Plaza, J.L.; Martín Rodríguez, E.; García Solé, J. Nanoparticles for Photothermal Therapies. *Nanoscale* **2014**, *6*, 9494–9530.
5. Duan, S.; Hu, Y.; Zhao, Y.; Tang, K.; Zhang, Z.; Liu, Z.; Wang, Y.; Guo, H.; Miao, Y.; Du, H.; et al. Nanomaterials for Photothermal Cancer Therapy. *RSC Adv.* **2023**, *13*, 14443–14460.
6. Liu, G.; Yan, C.; Kuang, D.; Song, L. Broadband Optical Absorption and Photothermal Properties of Partially Disordered $MoSe_2$ Nanospheres. *Mater. Chem. Phys.* **2023**, *293*, 126948.
7. Yu, X.; Fan, S.; Zhu, B.; El-Hout, S.I.; Zhang, J.; Chen, C. Recent Progress on Photothermal Nanomaterials: Design, Mechanism, and Applications. *Green Energy Environ.* **2024**, doi:10.1016/j.gee.2024.09.002.
8. Lamiel, C.; Hussain, I.; Warner, J.H.; Zhang, K. Beyond Ti-Based MXenes: A Review of Emerging Non-Ti Based Metal-MXene Structure, Properties, and Applications. *Mater. Today* **2023**, *63*, 313–338.
9. Wang, L.; Jiang, X.; Ji, Y.; Bai, R.; Zhao, Y.; Wu, X.; Chen, C. Surface Chemistry of Gold Nanorods: Origin of Cell Membrane Damage and Cytotoxicity. *Nanoscale* **2013**, *5*, 8384–8391.
10. Chen, D.; Miao, B.; Zhu, G.; Liang, Y.; Wang, C. Controllable Synthesis and Biomedical Applications of Bismuth-Based Nanospheres: Enhanced Photothermal Therapy and CT Imaging Efficiency. *Nanoscale* **2025**, *17*, 2281–2291.
11. Chithrani, B.D.; Ghazani, A.A.; Chan, W.C.W. Determining the Size and Shape Dependence of Gold Nanoparticle Uptake into Mammalian Cells. *Nano Lett.* **2006**, *6*, 662–668.
12. Foroozandeh, P.; Aziz, A.A. Insight into Cellular Uptake and Intracellular Trafficking of Nanoparticles. *Nanoscale Res. Lett.* **2018**, *13*, 339.
13. Lu, B.; Wang, J.; Hendriks, A.J.; Nolte, T.M. Clearance of Nanoparticles from Blood: Effects of Hydrodynamic Size and Surface Coatings. *Environ. Sci. Nano* **2024**, *11*, 406–417.
14. Rejman, J.; Oberle, V.; Zuhorn, I.S.; Hoekstra, D. Size-Dependent Internalization of Particles via the Pathways of Clathrin- and Caveolae-Mediated Endocytosis. *Biochem J.* **2004**, *377*, 159–169.

 doi:10.20944/preprints202505.0873.v1

15. Tsai, M.-F.; Chang, S.-H.G.; Cheng, F.-Y.; Shanmugam, V.; Cheng, Y.-S.; Su, C.-H.; Yeh, C.-S. Au Nanorod Design as Light-Absorber in the First and Second Biological near-Infrared Windows for in Vivo Photothermal Therapy. *ACS Nano* **2013**, *7*, 5330–5342.
16. Hong, G.; Antaris, A.L.; Dai, H. Near-Infrared Fluorophores for Biomedical Imaging. *Nat. Biomed. Eng.* **2017**, *1*, 0010.
17. Zhang, Z.; Du, Y.; Shi, X.; Wang, K.; Qu, Q.; Liang, Q.; Ma, X.; He, K.; Chi, C.; Tang, J.; et al. NIR-II Light in Clinical Oncology: Opportunities and Challenges. *Nat. Rev. Clin. Oncol.* **2024**, *21*, 449–467.
18. He, S.; Song, J.; Qu, J.; Cheng, Z. Crucial Breakthrough of Second near-Infrared Biological Window Fluorophores: Design and Synthesis toward Multimodal Imaging and Theranostics. *Chem. Soc. Rev.* **2018**, *47*, 4258–4278.
19. Tselikov, G.I.; Ermolaev, G.A.; Popov, A.A.; Tikhonowski, G.V.; Panova, D.A.; Taradin, A.S.; Vyshnevyy, A.A.; Syuy, A.V.; Klimentov, S.M.; Novikov, S.M.; et al. Transition Metal Dichalcogenide Nanospheres for High-Refractive-Index Nanophotonics and Biomedical Theranostics. *Proc. Natl. Acad. Sci. U. S. A.* **2022**, *119*, e2208830119.
20. Chernikov, A.S.; Tselikov, G.I.; Gubin, M.Y.; Shesterikov, A.V.; Khorkov, K.S.; Syuy, A.V.; Ermolaev, G.A.; Kazantsev, I.S.; Romanov, R.I.; Markeev, A.M.; et al. Tunable Optical Properties of Transition Metal Dichalcogenide Nanoparticles Synthesized by Femtosecond Laser Ablation and Fragmentation. *J. Mater. Chem. C* **2023**, *11*, 3493–3503.
21. Tselikov, G.; Minnekhanov, A.; Ermolaev, G.; Tikhonowski, G.; Kazantsev, I.; Dyubo, D.; Panova, D.; Tselikov, D.; Popov, A.; Mazitov, A.; et al. Tunable Nanostructuring for van der Waals Materials. *arXiv:2411.14060* 2024.
22. Ushkov, A.; Dyubo, D.; Belozerova, N.; Kazantsev, I.; Yakubovsky, D.; Syuy, A.; Tikhonowski, G.V.; Tselikov, D.; Martynov, I.; Ermolaev, G.; et al. Tungsten Diselenide Nanoparticles Produced via Femtosecond Ablation for SERS and Theranostics Applications. *Nanomaterials* **2024**, *15*, 4.
23. Vyshnevyy, A.A.; Ermolaev, G.A.; Grudinin, D.V.; Voronin, K.V.; Kharichkin, I.; Mazitov, A.; Kruglov, I.A.; Yakubovsky, D.I.; Mishra, P.; Kirtaev, R.V.; et al. Van der Waals Materials for Overcoming Fundamental Limitations in Photonic Integrated Circuitry. *Nano Lett.* **2023**, *23*, 8057–8064.
24. Ermolaev, G.A.; Stebunov, Y.V.; Vyshnevyy, A.A.; Tatarkin, D.E.; Yakubovsky, D.I.; Novikov, S.M.; Baranov, D.G.; Shegai, T.; Nikitin, A.Y.; Arsenin, A.V.; et al. Broadband Optical Properties of Monolayer and Bulk MoS_2. *npj 2D Mater. Appl.* **2020**, *4*, 21.
25. Munkhbat, B.; Wróbel, P.; Antosiewicz, T.J.; Shegai, T.O. Optical Constants of Several Multilayer Transition Metal Dichalcogenides Measured by Spectroscopic Ellipsometry in the 300-1700 Nm Range: High Index, Anisotropy, and Hyperbolicity. *ACS Photonics* **2022**, *9*, 2398–2407.
26. Yang, X.; Stein, E.W.; Ashkenazi, S.; Wang, L.V. Nanoparticles for Photoacoustic Imaging. *Wiley Interdiscip Rev. Nanomed. Nanobiotechnol.* **2009**, *1*, 360–368.
27. Li, W.; Chen, X. Gold Nanoparticles for Photoacoustic Imaging. *Nanomedicine* **2015**, *10*, 299–320.
28. Fu, Q.; Sun, W. Mie Theory for Light Scattering by a Spherical Particle in an Absorbing Medium. *Appl. Opt.* **2001**, *40*, 1354–1361.
29. Rastinehad, A.R.; Anastos, H.; Wajswol, E.; Winoker, J.S.; Sfakianos, J.P.; Doppalapudi, S.K.; Carrick, M.R.; Knauer, C.J.; Taouli, B.; Lewis, S.C.; et al. Gold Nanoshell-Localized Photothermal Ablation of Prostate Tumors in a Clinical Pilot Device Study. *Proc. Natl. Acad. Sci. U.S.A.* **2019**, *116*, 18590–18596.
30. Yang, L.; Liu, Y.; Wang, Q.; Shi, H.; Li, G.; Zhang, L. The Plasmon Resonance Absorption of Ag/SiO_2 Nanocomposite Films. *Microelectron. Eng.* **2003**, *66*, 192–198.
31. Barnes, W.L. Particle Plasmons: Why Shape Matters. *Am. J. Phys.* **2016**, *84*, 593–601.
32. Hale, G.M.; Querry, M.R. Optical Constants of Water in the 200-Nm to 200-Microm Wavelength Region. *Appl. Opt.* **1973**, *12*, 555–563.
33. Ermolaev, G.; Voronin, K.; Baranov, D.G.; Kravets, V.; Tselikov, G.; Stebunov, Y.; Yakubovsky, D.; Novikov, S.; Vyshnevyy, A.; Mazitov, A.; et al. Topological Phase Singularities in Atomically Thin High-Refractive-Index Materials. *Nat. Commun.* **2022**, *13*, 2049.

 doi:10.20944/preprints202505.0873.v1

34. Panova, D.A.; Tselikov, G.I.; Ermolaev, G.A.; Syuy, A.V.; Zimbovskii, D.S.; Kapitanova, O.O.; Yakubovsky, D.I.; Mazitov, A.B.; Kruglov, I.A.; Vyshnevyy, A.A.; et al. Broadband Optical Properties of Ti_3C_2 MXene Revisited. *Opt. Lett.* **2024**, *49*, 25–28.
35. Pflüger, J.; Fink, J.; Weber, W.; Bohnen, K.P.; Crecelius, G. Dielectric Properties of TiC_x,TiN_x,VC_x, and VN_x from 1.5 to 40 eV Determined by Electron-Energy-Loss Spectroscopy. *Phys. Rev. B* **1984**, *30*, 1155–1163.
36. Zograf, G.P.; Petrov, M.I.; Makarov, S.V.; Kivshar, Y.S. All-Dielectric Thermonanophotonics. *Adv. Opt. Photonics* **2021**, *13*, 643–702.
37. Zhao, L.; Zhang, X.; Wang, X.; Guan, X.; Zhang, W.; Ma, J. Recent Advances in Selective Photothermal Therapy of Tumor. J Nanobiotechnology 2021, 19, 335.
38. Volkov, V.; Slavich, A.; Ermolaev, G.; Pak, N.; Grudinin, D.; Kravtsov, K.; Tatmyshevskiy, M.; Semkin, V.; Syuy, A.; Mazitov, A.; et al. All-in-One van der Waals Material for Light Detection, Guiding and Modulation. *Research Square* 2025.
39. Naik, G.V.; Shalaev, V.M.; Boltasseva, A. Alternative Plasmonic Materials: Beyond Gold and Silver. *Adv. Mater.* **2013**, *25*, 3264–3294.
40. Jiang, W.; Fu, Q.; Wei, H.; Yao, A. TiN Nanoparticles: Synthesis and Application as near-Infrared Photothermal Agents for Cancer Therapy. *J. Mater. Sci.* **2019**, *54*, 5743–5756.
41. Grabowska-Jadach, I.; Kalinowska, D.; Drozd, M.; Pietrzak, M. Synthesis, Characterization and Application of Plasmonic Hollow Gold Nanoshells in a Photothermal Therapy-New Particles for Theranostics. Biomed. Pharmacother. 2019, 111, 1147–1155.
42. Oldenburg, S.J.; Averitt, R.D.; Westcott, S.L.; Halas, N.J. Nanoengineering of Optical Resonances. *Chem. Phys. Lett.* **1998**, *288*, 243–247.
43. VahidMohammadi, A.; Rosen, J.; Gogotsi, Y. The World of Two-Dimensional Carbides and Nitrides (MXenes). *Science* **2021**, *372*, eabf1581.
44. Jastrzębska, A.M.; Szuplewska, A.; Wojciechowski, T.; Chudy, M.; Ziemkowska, W.; Chlubny, L.; Rozmysłowska, A.; Olszyna, A. In Vitro Studies on Cytotoxicity of Delaminated TiC MXene. J. Hazard. Mater. 2017, 339, 1–8.
45. Gjerding, M.N.; Petersen, R.; Pedersen, T.G.; Mortensen, N.A.; Thygesen, K.S. Layered van der Waals Crystals with Hyperbolic Light Dispersion. *Nat. Commun.* **2017**, *8*, 320.
46. Gjerding, M.N.; Pandey, M.; Thygesen, K.S. Band Structure Engineered Layered Metals for Low-Loss Plasmonics. *Nat. Commun.* **2017**, *8*, 15133.
47. Black, J. Biological Performance of Tantalum. Clin. Mater. 1994, 16, 167–173.
48. Liu, Y.; Ji, X.; Liu, J.; Tong, W.W.L.; Askhatova, D.; Shi, J. Tantalum Sulfide Nanosheets as a Theranostic Nanoplatform for Computed Tomography Imaging-Guided Combinatorial Chemo-Photothermal Therapy. Adv. Funct. Mater. 2017, 27, 1703261.
49. Meier, M.; Wokaun, A. Enhanced Fields on Large Metal Particles: Dynamic Depolarization. *Opt. Lett.* **1983**, *8*, 581–583.
50. Rasskazov, I.L.; Zakomirnyi, V.I.; Utyushev, A.D.; Carney, P.S.; Moroz, A. Remarkable Predictive Power of the Modified Long Wavelength Approximation. *J. Phys. Chem. C* **2021**, *125*, 1963–1971.
51. Khurgin, J.B. How to Deal with the Loss in Plasmonics and Metamaterials. *Nat Nanotechnol* **2015**, *10*, 2–6.
52. Yakubovsky, D.I.; Arsenin, A.V.; Stebunov, Y.V.; Fedyanin, D.Y.; Volkov, V.S. Optical Constants and Structural Properties of Thin Gold Films. *Opt Express* **2017**, *25*, 25574–25587.
53. Hu, B.Y.-K. Kramers–Kronig in Two Lines. *Am. J. Phys.* **1989**, *57*, 821–821.